Synthesis, Crystal Structure, and Computational Investigations of 2-(2-(4-Fluorophenyl)-2-oxoethyl)-6-methyl-5-(4-methylbenzyl)pyridazin-3(2*H*)-one as Antiviral Agent

Fouad El Kalai [1], **Christina Susan Abraham** [2], **Sevgi Kansiz** [3], **Afaf Oulmidi** [4], **Sambantham Muthu** [5], **Johanan Christian Prasana** [2], **Necmi Dege** [6], **Hatem A. Abuelizz** [7], **Rashad Al-Salahi** [7], **Noureddine Benchat** [1] and **Khalid Karrouchi** [8,*]

[1] Laboratory of Applied Chemistry and Environment (LCAE), Department of Chemistry, Faculty of Sciences, Mohammed I University, Oujda 60000, Morocco; f.elkalai@ump.ac.ma (F.E.K.); noureddinebenchat@gmail.com (N.B.)

[2] Department of Physics, Madras Christian College, East Tambaram 600059, India; christinaaruvickal@gmail.com (C.S.A.); jcprasana@mcc.edu.in (J.C.P.)

[3] Department of Fundamental Sciences, Faculty of Engineering, Samsun University, Samsun 55420, Turkey; sevgi.kansiz@samsun.edu.tr

[4] Institute of Condensed Matter and Nanosciences, Molecular Chemistry, Materials and Catalysis (IMCN/MOST), Université Catholique de Louvain, 1348 Louvain-la-Neuve, Belgium; afaf.oulmidi@uclouvain.be

[5] Department of Physics, Arignar Anna Government Arts College, Cheyyar 604407, India; mutgee@gmail.com

[6] Department of Physics, Faculty of Arts and Sciences, Ondokuz Mayıs University, Samsun 55139, Turkey; necmid@omu.edu.tr

[7] Department of Pharmaceutical Chemistry, College of Pharmacy, King Saud University, P.O. Box 2457, Riyadh 11451, Saudi Arabia; habuelizz@ksu.edu.sa (H.A.A.); ralsalahi@ksu.edu.sa (R.A.-S.)

[8] Laboratory of Analytical Chemistry and Bromatology, Team of Formulation and Quality Control of Health Products, Faculty of Medicine and Pharmacy, Mohammed V University in Rabat, Rabat 10100, Morocco

* Correspondence: khalid.karrouchi@um5s.net.ma

Abstract: The aim of this work was to scrutinize the physiochemical properties of a new pyridazin-3(2*H*)-one derivative with potential pharmaceutical effectiveness via density functional theory (DFT) and molecular docking analysis. The compound 2-(2-(4-fluorophenyl)-2-oxoethyl)-6-methyl-5-(4-methylbenzyl)pyridazin-3(2*H*)-one (FOMMP) was synthesized and characterized by FT-IR, UV-Vis, ^{1}H-NMR, ^{13}C-NMR, ESI-MS, and single-crystal XRD analysis. In addition, the geometrical structure of the molecule was analyzed. Frontier molecular orbital (FMO) analysis showed a low energy gap that suggests the chemical reactivity of the title compound. The electrophilicity index (ω) points towards the probable biological activity of FOMMP. The molecular electrostatic potential (MEP) was used to assess the local reactivity properties and suggests that the nitrogen atom sites are electronegative. Computational and experimental UV-spectral analyses were performed to attain the bandgap associated with electronic transitions while the charge transfer length helped us determine that the excitation mode associated with the electronic transitions is long-ranged. Natural hybrid orbital (NHO) and natural bond orbital (NBO) analyses depicted the prominent acceptor-donor interactions in terms of the stabilization energies. Hirshfeld surface analysis was performed to analyze the intermolecular interactions in the crystal structure. In addition, a molecular docking study was executed to evaluate the potential of the protease inhibitors (PIs) against SARS-CoV-2.

Keywords: pyridazinone; crystal structure; DFT; SARS-CoV-2; molecular docking

1. Introduction

Heterocyclic compounds, in particular pyridazine derivatives, have attracted great interest from researchers for many years due to their wide range of biological and pharmacological properties, including antiviral [1,2], antimicrobial [3,4], antitubercular [5],

analgesic and anti-inflammatory [6,7], anticancer [8], anti-HIV [9], anti-Alzheimer [10], antihypertensive [11], anticonvulsant [12], and antileishmanial activities [13]. Thus, several pyridazinone derivatives have been commercialized as agrochemical agents, such as herbicides, fungicides, and insecticides [14–17]. On the other hand, in order to examine the influence of different substituents on the structures and to reveal the relationship of these groups with their biological properties, the determinations of the geometrical and structural properties of these derivatives have become essential. Recently, DFT calculations have become a very important and commonly used tool in developing a relationship between experimental and theoretical data by providing evidence related to molecular geometry, electrical and spectroscopic properties, and also in predicting the properties of molecules with a high accuracy [18–25]. In the present study, new pyridazinone compound, i.e., 2-(2-(4-fluorophenyl)-2-oxoethyl)-6-methyl-5-(4-methylbenzyl)pyridazin-3(2*H*)-one (FOMMP), was prepared and identified using FT-IR, UV-Vis, ^{1}H-NMR, ^{13}C-NMR, and mass spectrometry (Scheme 1), and the molecular structure of FOMMP was confirmed by single-crystal XRD analysis. In addition, the geometrical structure, FMO analysis, electrophilicity index (ω), and MEP, NBO, and NHO analyses of FOMMP were carried out using the DFT/B3LYP method with a 6-311++ G (d,p) basis set. In addition, a docking study was performed to explore the potential of the studied molecules against the SARS-CoV-2 disease through the study of their binding modes to the active site of protein 5R82.
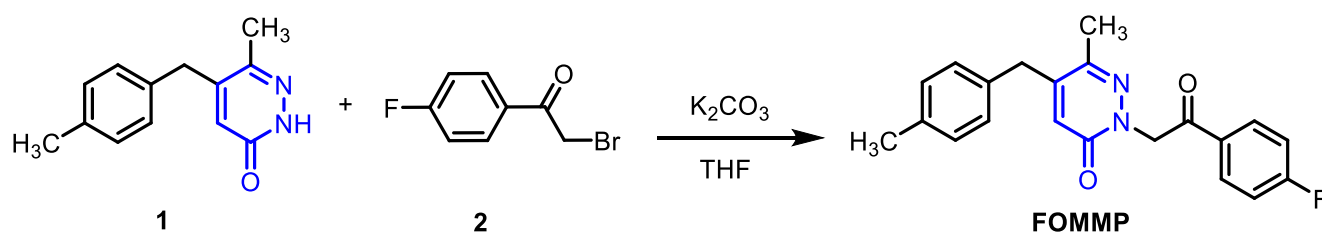
Scheme 1. Synthetic route for the preparation of FOMMP.

2. Materials and Methods

2.1. Materials and Instruments

Reactions were checked with TLC using aluminum sheets with silica gel 60 F254 (Merck, Darmstadt, Germany). Melting points were measured using a Buchi-Tottoli apparatus (Flawil, Switzerland). The FT-IR spectrum was recorded with Perkin-Elmer Fourier Transformer FT Pargamon 1000 PC Spectrophotometer (400–4000 cm^{-1}) (Shelton, CT, USA). ^{1}H and ^{13}C NMR spectra were recorded in CDCl$_3$ on a Bruker spectrometer (Switzerland). Mass spectra were collected using the API 3200 LC/MS/MS system (Framingham, MA, USA), equipped with an ESI source.

2.2. Synthesis Procedure for the Preparation of FOMMP

The FOMMP compound was synthesized following the reported procedure [26–29]. To a mixture of pyridazinone (**1**) (3 mmol) in 20 mL of THF, potassium carbonate (9 mmol) and 10% of tetrabutylammonium bromide (TBAB) were added as catalyst. The reaction mixture was refluxed for 1 h. After cooling, 2-bromo-1-(4-fluorophenyl)ethan-1-one (**2**) (3.2 mmol) was added dropwise and the mixture was refluxed for 6 h. The reaction mixture was filtered, the solvent was removed, and the residue was purified by chromatography on a silica column (Eluent: ethyl acetate/hexane: 5/5) to give the product (FOMMP). Yellow crystals produced the following yield = 67%, mp = 154–156 °C; ^{1}H NMR (300 MHz, CDCl$_3$, δ (ppm)): 1.48 (s, 3H, CH$_3$); 2.19 (s, 3H, CH$_3$); 3.72 (s, 2H, -CH$_2$-), 5.54 (s, 2H, –CH$_2$CO); 6.55 (s, 1H, H-pyridazinone); 7.10-8.25 (m, 8H, H–Ar). ^{13}C NMR (75 MHz, CDCl$_3$) δ, ppm: 19.29; 21.20; 38.34; 57.62; 77.71; 128.61; 128.92; 129.02; 129.61; 129.86; 129.92; 130.50; 133.37; 134.67; 135.74; 137.75; 146.29; 147.52; 161.68, 193.22. MS-ESI+: *m/z* = 351.2 [M+H]$^+$, 373.0 [M+Na]$^+$.

2.3. X-ray Analysis

X-ray data collection and structure refinement were conducted according to the literature [30–33]. A summary of the cell parameters, data collection, solution structures, and the refinement of the crystal structure are provided in Table 1. The corresponding crystallographic data were deposited with the Cambridge Crystallographic Data Centre as supplementary publications. CCDC 1960994.

2.4. Computational Details

DFT calculations were performed using the Gaussian 09W software, and physicochemical calculations were performed using the B3LYP method with the 6-311++ G (d,p) basis set [34,35]. Initial geometric optimization was carried out to find the minimum energy configuration of the compound. The wave function and energy were calculated at the starting geometry and then we proceeded until the lowest energy was found. The absence of imaginary frequencies points towards the attainment of an energy minimum. The electron localization function was used to study the chemical bonding between the atoms of FOMMP. The orbital contribution in terms of the density of states was analyzed using the GaussSum software [36]. TD-DFT in DMSO solution was considered to analyze the electronic absorption spectrum of the title molecule. Transfer of charges within the molecule was explored with the Multiwfn 3.4.1 program: a wave function analyzer software. The NBO and NHO analysis helped comprehend the intra- and intermolecular hydrogen bonding, intermolecular charge transfer, and delocalization of the electron density of FOMMP. An insight into the reactivity of FOMMP was studied in terms of the calculated hardness (η) values while an important CDFT parameter electrophilicity index (ω) was analyzed to obtain information about the probable biological activity. MEP analysis was employed to address the local reactivity properties of the compound. The Maestro program [37], also implemented in Schrödinger Materials Science Suite 2018-1, was used for the preparation of input files, the visualization of the results, and the calculation of drug-likeness parameters. The optimized structure was docked using AutoDock Tools (ADT) Version 1.5.6 [38].

3. Results

3.1. Description of Crystal Structure

Figure 1a shows the asymmetric unit of FOMMP and Table 1 summarizes the crystal data and structure refinement. There is one independent molecule in the asymmetric unit. In this crystal, FOMMP is not planar, the C1–C6 fluorophenyl ring is inclined to the pyridazin ring by 87.0(2)°, while the methylbenzyl and pyridazin rings are twisted for each other, making a dihedral angle of 89.8(2)°. The molecular structure is stabilized by the intermolecular C10–H10···O2 and C13–H13*B*···F1 hydrogen bonds (Figure 1b and Table 2). In the crystal, molecules are linked by a pair of C13–H13*B*···F1 hydrogen bonds forming inversion dimers. The dimers are linked by C10–H10···O2 hydrogen bonds forming chains along the *b*-axis direction. In the molecule, the C7–O1 and C9–O2 bond distances are essentially equivalent, i.e., 1.210(7) Å and 1.238(7) Å, respectively. These bond lengths are typical of double bonds.
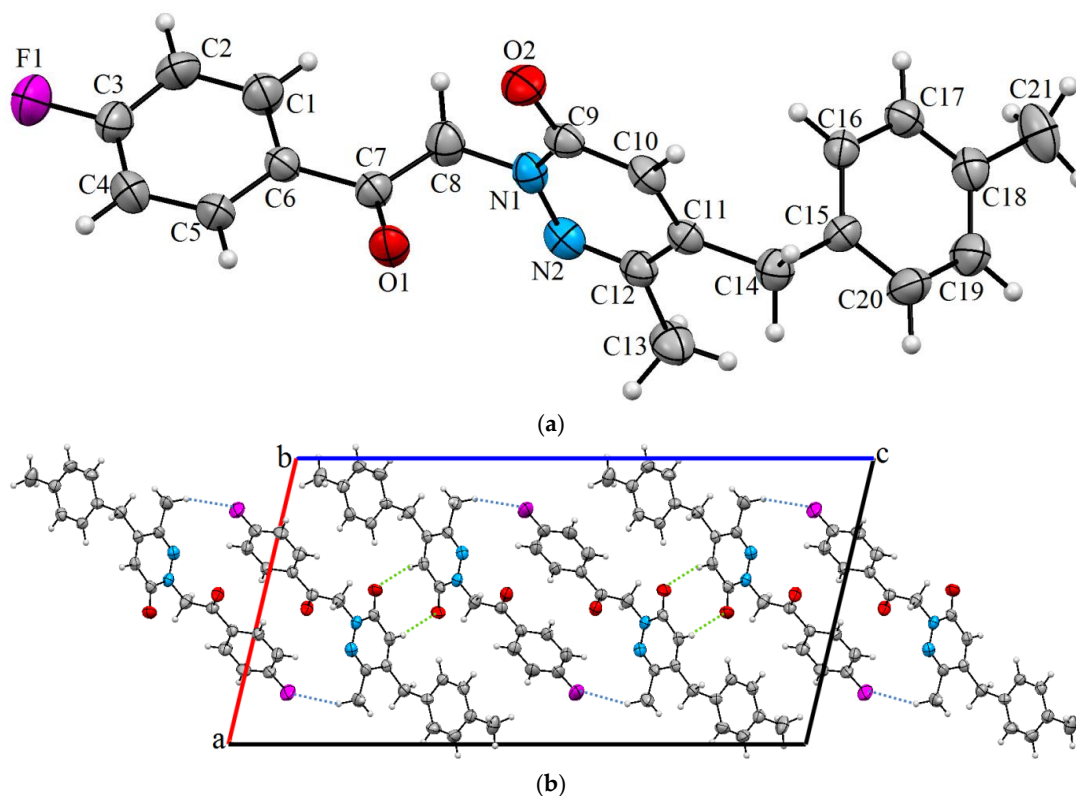
(a)

(b)

Figure 1. (**a**) Molecular structure of FOMMP. (**b**) A partial view of the crystal packing of FOMMP along the *b*-axis direction. Blue dashed lines denote the intermolecular C–H···F hydrogen bonds and green ones denote C–H···O hydrogen bonds.

Table 1. Crystallographic and refinement data for FOMMP.

CCDC Deposition Number	CCDC 1960994
Chemical formula	$C_{21}H_{19}FN_2O_2$
M_r	350.38
Crystal system, space group	Monoclinic, $P2_1/c$
Temperature (K)	296
a, b, c (Å)	13.7166 (15), 5.0232 (4), 27.016 (3)
β (°)	103.413 (8)
V (Å^3)	1810.6 (3)
Z	4
Radiation type	Mo $K\alpha$
μ (mm^{-1})	0.09
Crystal size (mm)	0.78 × 0.34 × 0.05
Data collection	
Diffractometer	STOE *IPDS* 2
Absorption correction	Intergration (X-RED32 [39])
T_{min}, T_{max}	0.980, 0.993
No. of measured, independent, and observed [$I > 2\sigma(I)$] reflections	10,673, 3174, 1320
R_{int}	0.084
$(\sin \theta/\lambda)_{max}$ (Å^{-1})	0.596
Refinement	
$R[F^2 > 2\sigma(F^2)]$, $wR(F^2)$, S	0.091, 0.334, 1.02
No. of reflections	3174
No. of parameters	236
H-atom treatment	H-atom parameters constrained
$\Delta\rho_{max}$, $\Delta\rho_{min}$ (e Å^{-3})	0.21, −0.29

Table 2. Hydrogen bond geometry (Å, °) for FOMMP.

D–*H*⋯*A*	*D*–*H*	*H*⋯*A*	*D*⋯*A*
C10–H10⋯O2 [i]	0.93	2.59	3.496(8)
C8–H8A⋯O1 [ii]	0.97	2.62	3.543(9)
C13–H13B⋯F1 [iii]	0.96	2.46	3.357(6)

Symmetry codes: (i) $-x + 1, y - 1/2, -z + 3/2$; (ii) $x, y + 1, z$; (iii) $-x + 1, -y + 1, -z + 1$.

3.2. Optimized Molecular Geometry

Figure 2 shows the optimized structure and the atom numbering of the title compound. The structure used in all subsequent analyses takes the optimized structure of this molecule into account. Let the ring systems C9–C10–C11–C12–C13–C14 and C20–C21–C22–C23–C24–C25 be designated as ring I and II, respectively. C–C bond lengths in benzene rings were observed to be 1.42 Å for ring I and in ring II. The presence of fluorine in the carbon skeleton of ring I caused a slight deviation in the C–C bond distance from the regular expected value, which is 1.393 ± 0.02 Å [40–42]. H–C–H angles varied between 108.8–110.8°. Angle C1–N6–C17 = 119.2°, which falls in an expected range of 119° [42] such that the asymmetry observed was due to interactions between C and N–H groups. Slight aberrations from the literature values can be attributed to the variations due to the least-square refinements and inverse overlap [43,44].
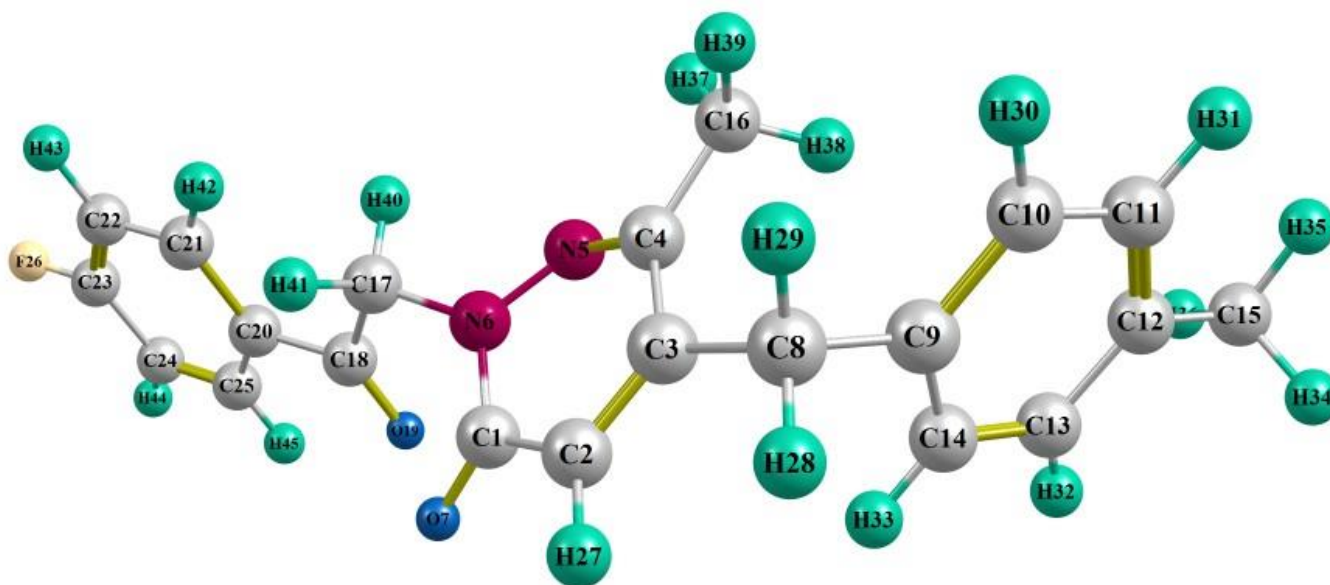
Figure 2. Optimized structure of FOMMP.

3.3. FT-IR Spectra Analysis

The vibrational spectral analysis of FOMMP was performed on the basis of the experimentally obtained FT-IR spectrum (Figure 3). In general, multiple bands are displayed in the spectral range 3100–3000 cm^{-1} by aromatic C-H stretching vibrations [45–50]. For FOMMP, the vibration bands observed between 2856 and 3083 cm^{-1} were attributed to the stretching modes of five CH groups in 4-methylbenzyl, 4-fluorobenzyl, and pyridazinone rings, in addition to two CH$_2$ bonds and one CH$_3$ bond. C–H in-plane deformation vibrations are generally observed as medium to weak bands in the 1300–1000 cm^{-1} region [45–48]. The C–H in-plane deformation vibration of the title compound was observed between 1017 and 1291 cm^{-1}. C–H out-of-plane deformations were reported in the region 600–900 cm^{-1} [45–48]. The C–H out-of-plane deformation vibration for FOMMP was observed at 840, 810, 731, 634, and 593 cm^{-1} with weak intensity [45–48]. The carbonyl (C=O) stretching vibrations appeared generally in the region 1600–1800 cm^{-1}, which is one of the most representative and intense bands in an infrared spectrum [45–48]. Daoui

et al. [46] and El Kalai et al. [47] reported the C=O stretching vibration in the pyridazinone ring at 1652 cm^{-1} and 1653 cm^{-1}, respectively. The ν(C=O) vibration of the title compound was observed at 1650 cm^{-1}. On the other hand, the band at 1599 cm^{-1} was attributed to C=N stretching vibration in the pyridazinone ring. This mode was reported at 1604 and 1606 cm^{-1} [48,49]. C=C stretching vibrations were attributed to bands in the interval in the region 1430–1625 cm^{-1} [45]. The C=C vibrations of the aromatic rings of the title compound were observed at 1552, 1509, 1460, and 1427 cm^{-1}.
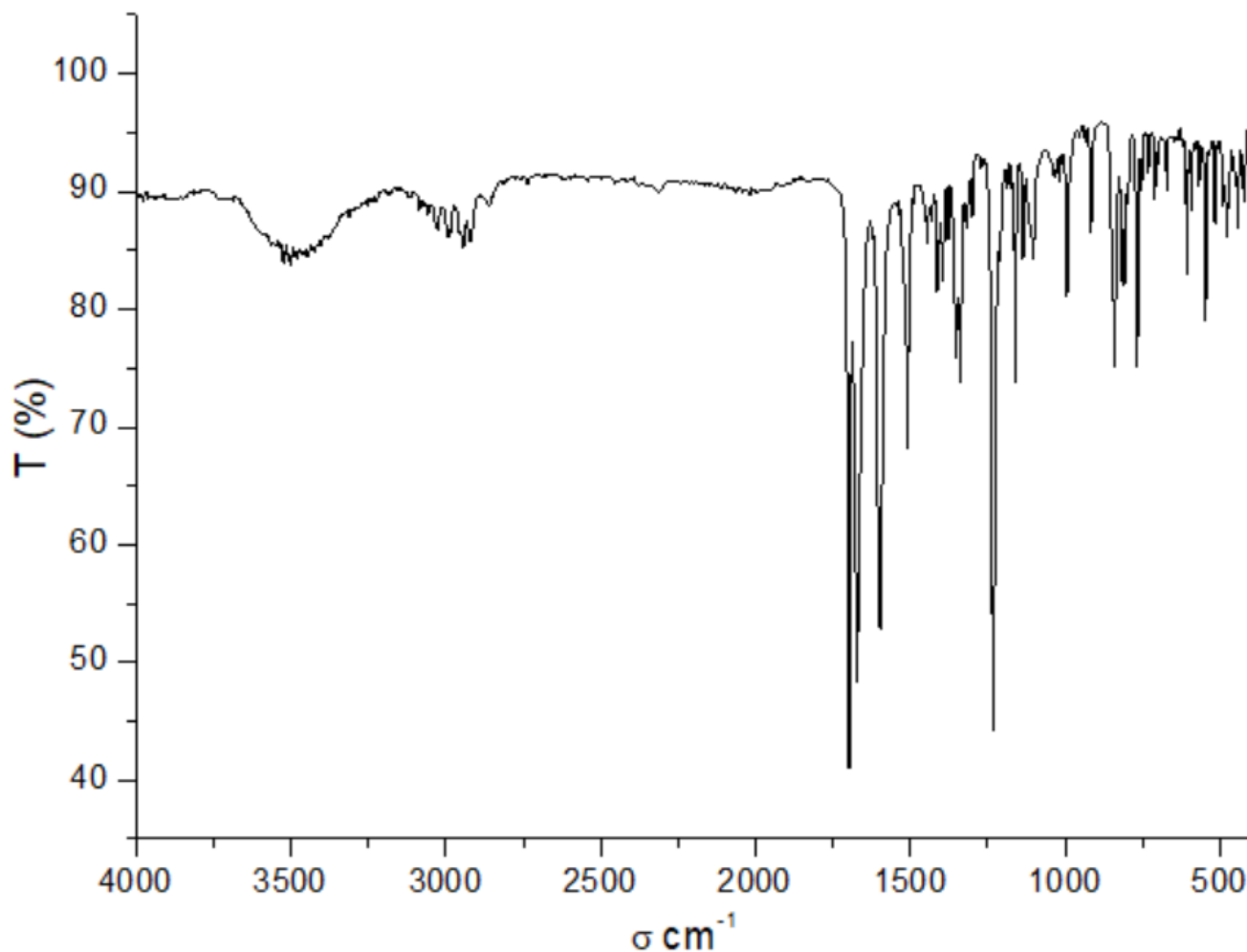

Figure 3. FT-IR spectrum of FOMMP.

3.4. NMR Spectra Analysis

The experimental ^{1}H and ^{13}C NMR spectra of FOMMP were obtained using DMSO-d_6 as a solvent (Figures S1 and S2 in Supplementary Materials). The proton NMR spectrum of FOMMP showed two singlets at δ = 2.28 and 2.37 ppm, which are characteristic of two CH$_3$ groups, and the two CH$_2$ groups resonate at δ = 3.79 and 5.57 ppm as two singlets. The H-4 proton of pyridazinone resonates at δ = 6.58 ppm as a singlet. The aromatic protons resonate as multiplets in the range δ = 7.03–8.07 ppm.

For carbon NMR spectrum, the signals at 193.22 and 161.68 ppm were attributed to two carbonyls (C=O). The C3, C4, and C5 carbons of the pyridazinone ring resonate at 146.29, 137.75, and 135.74 ppm. The signal at 147.52 ppm was assigned to the C–F group, and the aromatics carbon of FOMMP appeared in the range of 134.67–127.81 ppm. The signals at 38.34 and 57.62 ppm were attributed to two CH$_2$ groups and the signals at 19.29 and 21.20 ppm were attributed to two CH$_3$ groups.

3.5. ESI-MS Study

The ESI-MS spectrum of FOMMP displayed molecular ion peaks with m/z values of 351.2 and 373.0, corresponding to the molecular weights of $[M+H]^+$ and $[M+Na]^+$, respectively (Figure S3 in Supplementary Materials). These values are in good agreement with the proposed composition for FOMMP ($C_{21}H_{19}FN_2O_2$).

3.6. Hirshfeld Surface Analysis

In this study, the contributions of different intermolecular interactions to the crystal structure were investigated using Hirshfeld surface (HS) analysis. Figure 4 illustrates the Hirshfeld surface of FOMMP with mapped d_{norm}. The red spots on the HS indicate the intercontacts included in the intermolecular interactions [51–53]. Areas where neighboring atoms are too far apart to interact with each other are indicated by blue fields.
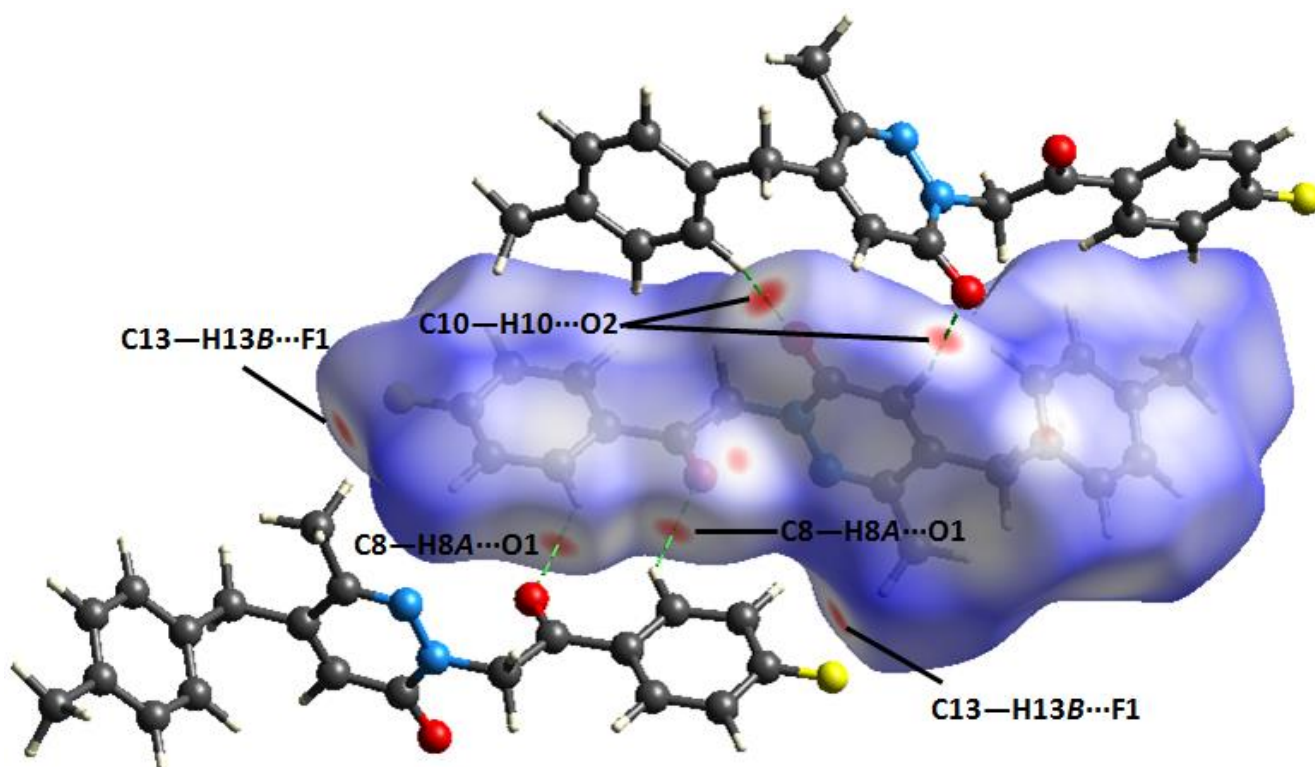

Figure 4. d_{norm} mapped on HS for the intercontacts of FOMMP.

The surfaces of 3D d_{norm} were plotted over a fixed color scale of -0.1843 (red) to 1.4882 (blue) with a standard (high) surface resolution. In Figure 4, the red circular collapsing on the d_{norm} surface of the FOMMP structure represents the C–H···O and C–H···F intermolecular interactions. The 2D fingerprint of the total contacts in HS is illustrated in Figure 5. The major contributions to the total HS are H···H interactions with 44.3%, which illustrates the 2D fingerprint of the (d_i, d_e) points related with H atoms in Figure 5. In Figure 5, two symmetrical wings on the left and right sides (21.9%) are shown on the graph of C···H/H···C interactions. In addition, there are O···H/H···O (15%), F···H/H···F (10.5%), and N···H/H···N (3.6%) contacts.
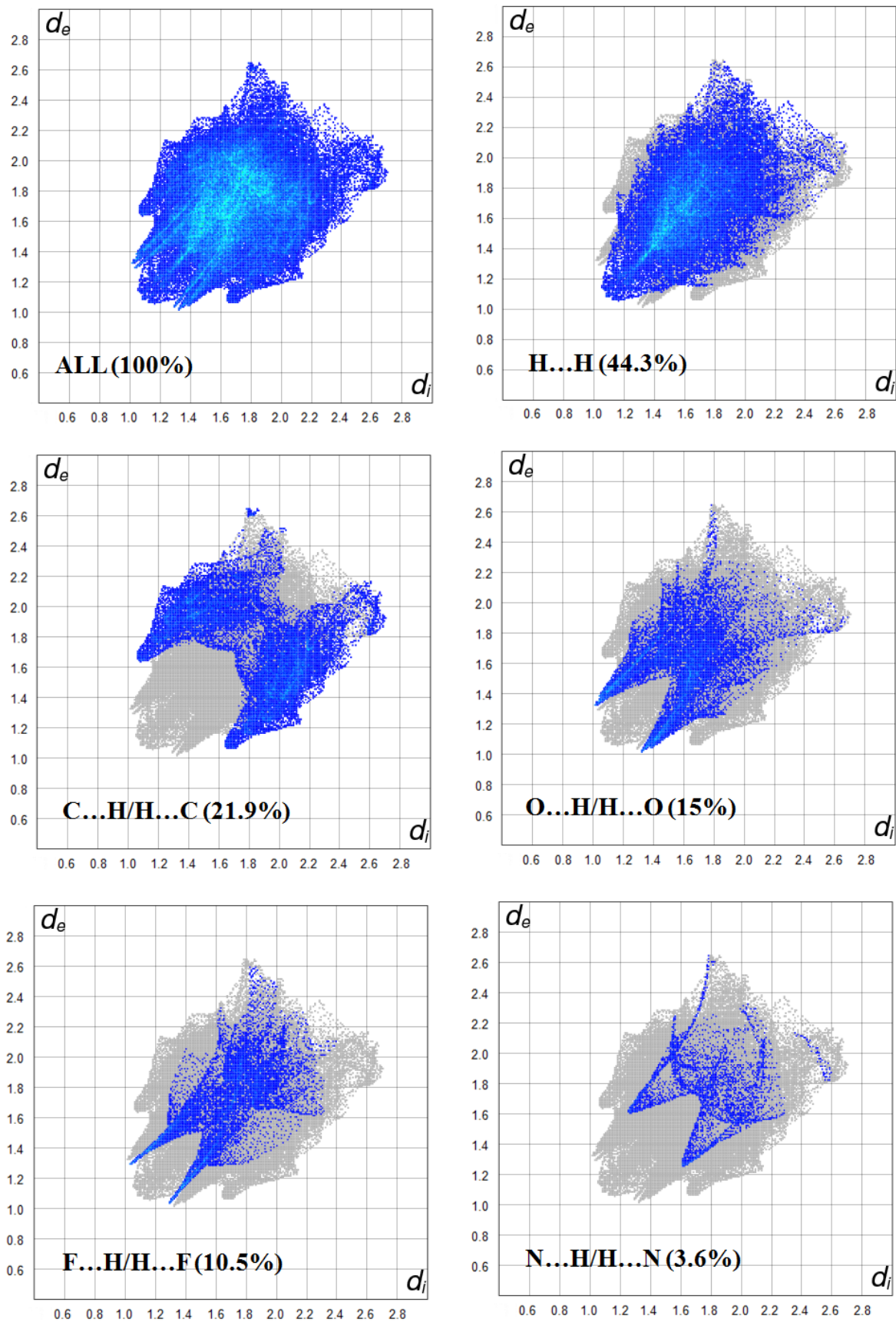
Figure 5. Finger plots of FOMMP.

3.7. Frontier Molecular Orbitals (FMOs) Analysis

FMO analysis is suitable to attain details on the reactivity and stability associated with the title compound [54,55]. HOMO, LUMO energies, and the energy gap were −6.19, −1.863, and 4.327 eV, respectively, and are represented in Figure 6. The calculated energy values of FOMMP are seen in Table 3. A considerably low energy gap suggests chemical reactivity associated with FOMMP [56]. A hardness η of 2.164 eV defines the degree of resistance to the distortion in electronic configuration [57,58] in the molecule while an electronegativity χ calculated to be 4.027 eV explicates the affinity of the selected molecule towards electrons [59]. Compared with the available literature [60,61], it can, thus, be concluded that the η value in this molecule demonstrates that it is not a very hard molecule. This, in turn, is associated with greater reactivity due to an amplified sensitivity towards the transfer of charges [62]. In addition, the electrophilicity index ω (3.747 eV) falls in a region that suggests the title molecule is biologically active [63]. These reactivity and bioactivity descriptors behave as a precursor in scrutinizing the title compound further for its biological activity in terms of molecular docking.
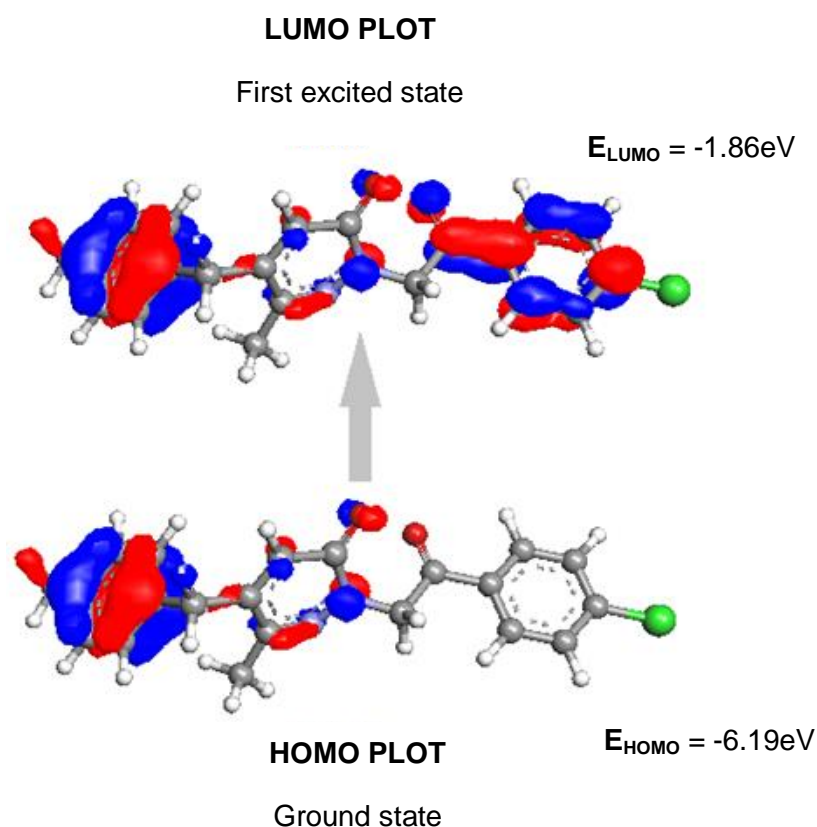
LUMO PLOT

First excited state

E_{LUMO} = -1.86eV

E_{HOMO} = -6.19eV

HOMO PLOT

Ground state

Figure 6. Frontier molecular orbital depiction of FOMMP.

Table 3. Calculated energy values of FOMMP.

Molecular Properties	E_{HOMO}	E_{LOMO}	E_{HOMO-1}	E_{LUMO+1}	E_{HUMO-2}	E_{LUMO+2}
Energy (eV)	−6.19	−1.863	6.460	1.777	6.701	1.163
Energy Gap (eV)	4.327		4.683		5.538	
Ionization Potential (I)	6.190		6.460		6.701	
Electron Affinity (A)	1.863		1.777		1.162	
Global Hardness (η)	2.164		2.341		2.770	
Electro negativity (χ)	4.027		4.118		3.932	
Global Softness (σ)	0.231		0.214		0.181	
Chemical Potential (μ)	−4.027		−4.118		−3.932	
Global Electrophilicity (ω)	3.747		3.621		2.792	

The DOS spectrum as seen in Figure 7 depicts the available states to be occupied by electrons for an energy range of -20 to 20 eV. The maximum number of states available to be occupied by electrons in the positive and negative domains corresponds to $\approx$11.5 eV and 3.5 eV along the negative and positive axes, respectively.
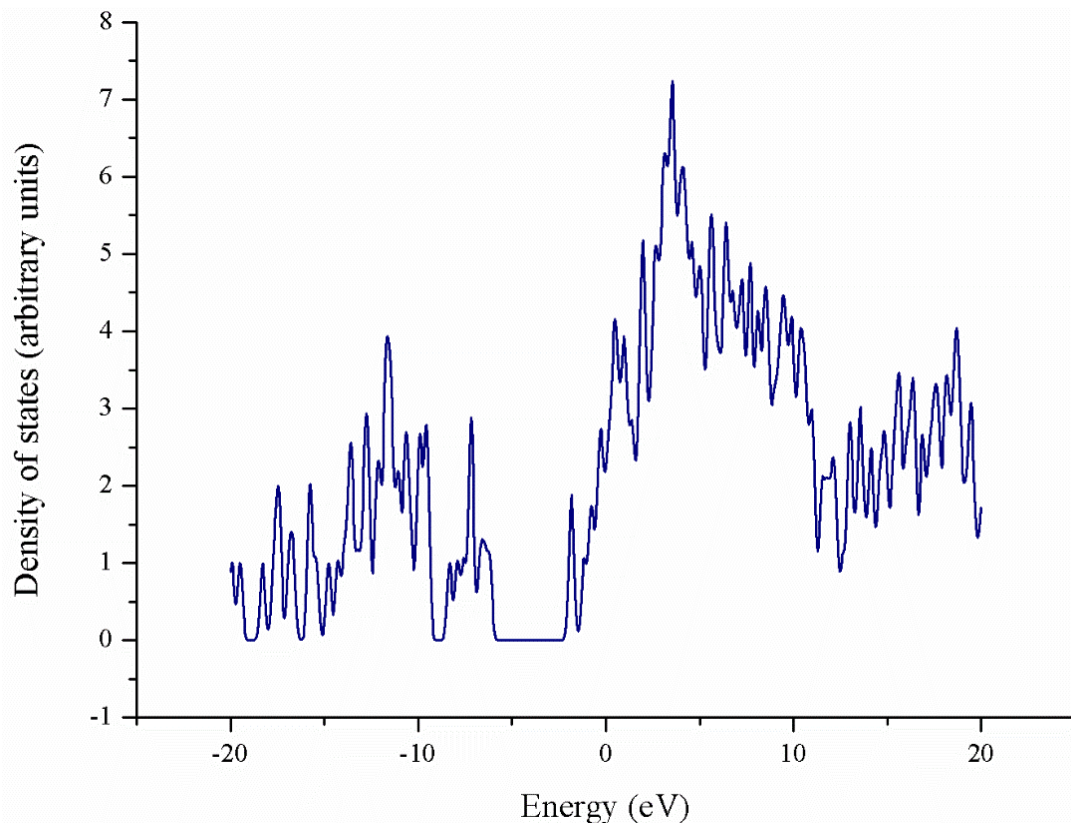

Figure 7. Calculated DOS of FOMMP.

3.7.1. Charge Transfer and Excitation Analysis

Details about D, S, and the excitation energy of the first three excited states: S1, S2, and S3, are presented in Table 4, while the electron–hole (represented by green–blue, respectively) distribution is represented in Figure 8. The value of Δr, which is the numerical gauge of the electron excitation mode [64] in the title molecule, was greater than 2 Å. This suggests that the molecule exhibits long-range excitations corresponding to all three excitation states. From Table 4, it can be seen that the largest value of D and the smallest value of S is for S1, thereby indicating a greater CT length. In all three excited states, the electron and hole distribution observed in terms of the RSMD of the electron and hole values was maximum along the X direction (refer Table 4). The extent of separation between holes and electrons represented by the t-index suggests that, if the 't' value along any one direction is greater than zero, then sufficient spatial separation is present between holes and electrons [64]. In this molecule, the 't' index was detected to be greater than zero along the X direction, thus indicating a hole–electron spatial separation. This observation was in concurrence with data attained in terms of D and S values. On visualizing the hole–electron spatial separations, all three states can be seen to show significant spatial separation (refer to Figure 7).

Absorption based on the first three excited states: S1, S2, and S3, in the solvent phase is summarized in Table 5, which helped in identifying the regions that are most responsible for excitations within the title molecule. The theoretically obtained UV spectrum in the solvent phase (DMSO) is shown in Figure 9. The excitation mode with the maximum absorption wavelength (λ_{max} = 359.45 nm) was found to have oscillator strength (f = 0.0294).

Table 4. Overlap integral, charge transfer length, Δr, and excitation energy for different excited states of FOMMP.

Parameter	Excited States		
	S1	**S2**	**S3**
Overlap integral of electron–hole, S	0.02	0.08	0.08
Charge transfer length, D (Å)	11.09	6.00	8.16
Excitation energy, ΔE (eV)	3.45	3.72	3.93
RMSD of electron			
X	1.4	2.613	2.20
Y	1.33	1.30	1.34
Z	0.86	1.02	0.91
RMSD of hole			
X	2.52	2.03	3.08
Y	0.98	0.99	1.25
Z	0.78	0.83	1.00
t index			
X	9.131	3.61	5.52
Y	−1.09	−0.65	−1.22
Z	−0.67	−0.15	−0.94
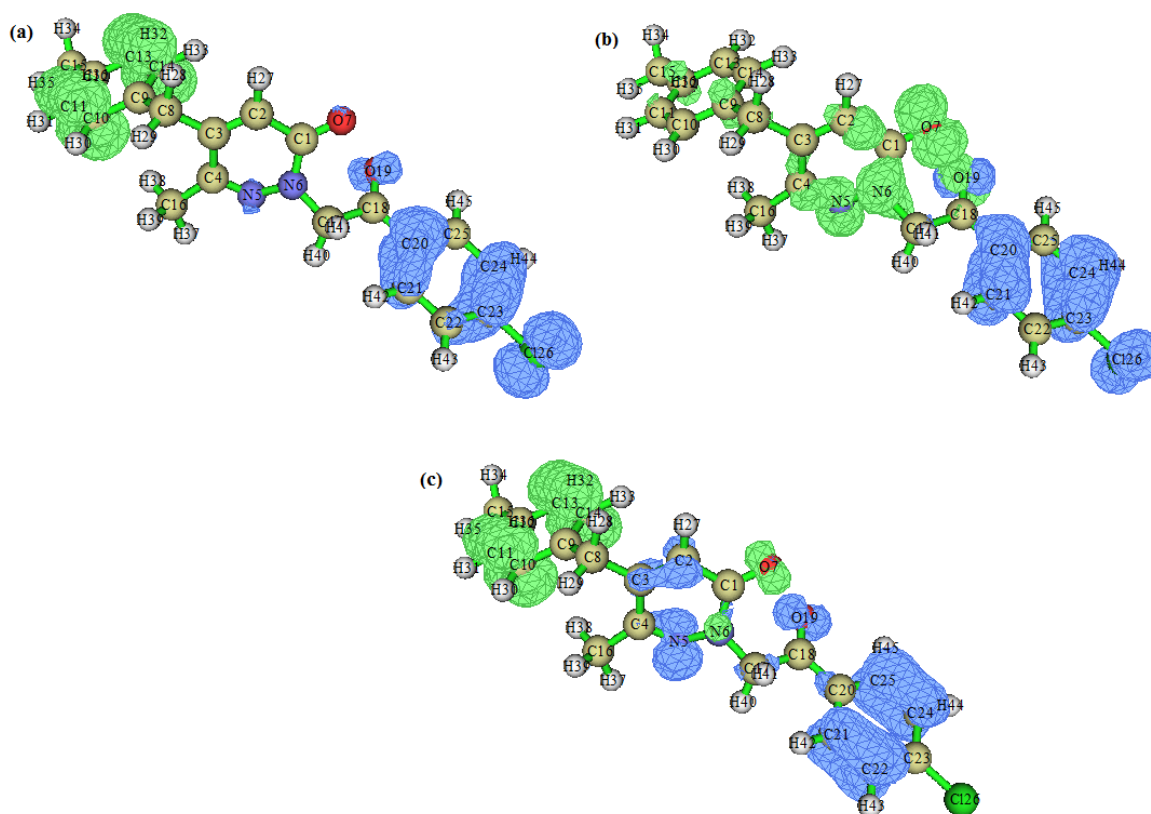
Figure 8. Electron–hole distribution for excited states (**a**) S_1, (**b**) S_2, and (**c**) S_3 of FOMMP (represented as green and blue isosurfaces, respectively).

The transition from HOMO to LUMO present in S1 has a bandgap of 3.452 eV in the solvent (DMSO) phase with a contribution of 77%. In the lower oscillator strength state, i.e., S2, details of transitions from HOMO to LUMO+1 and HOMO−2 to LUMO+1 are depicted with contributions of 31% and 54%, respectively. In S3, transitions from HOMO−2

to LUMO were seen to have a contribution of 53%, while HOMO−1 to LUMO showed a 30% contribution.

Table 5. Electronic properties of FOMMP at solvent phase.

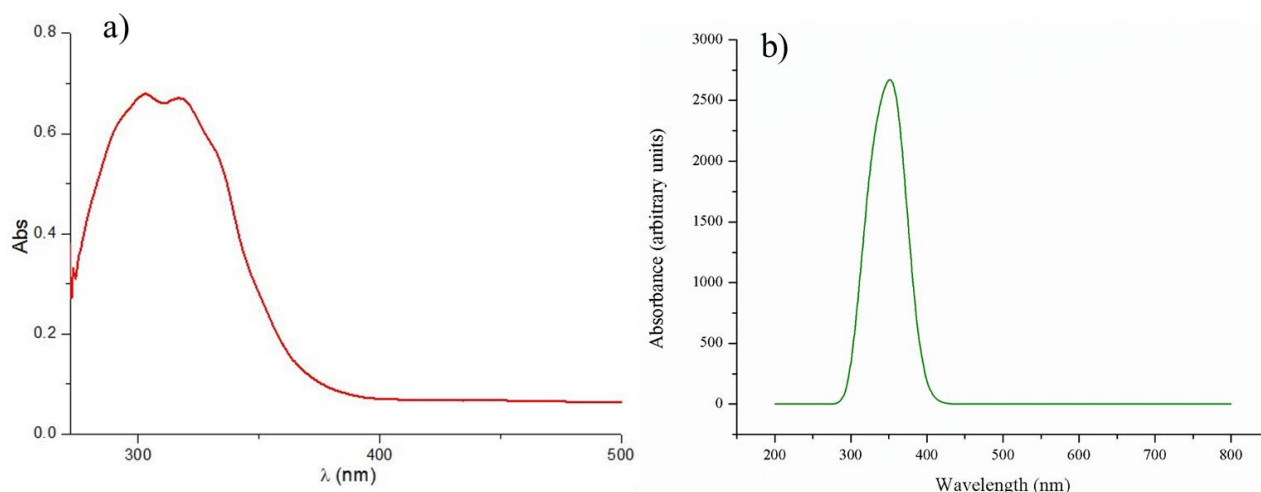| Excited States	Band Gap (eV)	Wavelength (nm)	Energy (cm^{-1})	Osc. Strength
1	3.452	359.445	27,820.67	0.029
2	3.719	333.629	29,973.38	0.021
3	3.937	315.142	31,731.68	0.010

Figure 9. Experimental (**a**) end simulated (**b**) UV-Vis absorption spectra of FOMMP.

3.7.2. Natural Bond Orbital Analysis

The stabilization energies (E2) of the donor–acceptor interactions of the title compound FOMMP were studied (Table S1 in Supplementary Materials). The following transitions showed significantly high stabilization energies and are, thus, responsible for the stabilization of the structure:

- π (C9–C10) transition to π* (C11–C12) and π* (C13–C14) has stabilization energies of 18.36 and 19.08 kJ/mol, respectively;
- π (C11–C12) transition to π* (C9–C10) and π* (C13–C14) has stabilization energies of 20.39 and 18.68 kJ/mol, respectively;
- π (C13–C14) transition to π* (C9–C10) and π* (C13–C14) has stabilization energies of 20.41 and 21.05 kJ/mol, respectively;
- π (C20–C21) transition to π* (C22–C23) and π* (C24–C25) has stabilization energies of 18.35 and 20.27 kJ/mol, respectively;
- π (C22–C23) transition to π* (C20–C21) and π* (C24–C25) has stabilization energies of 20.48 and 16.09 kJ/mol, respectively;
- π (C24–C25) transition to π* (C20–C21) and π* (C22–C23) has stabilization energies of 17.83 and 23.12 kJ/mol, respectively.

The aforementioned transitions with high stabilization energies correspond to only six pairs of orbitals, namely, (C9–C10), (C11–C12), and (C13–C14), and (C20–C21), (C22–C23), and (C24–C25), which form the ring structures I and II, respectively. These values predict that FOMMP has intensive donor–acceptor interactions within the ring structure. A few prominently observed lone pair (LP) transitions are associated with the following:

- LP(1) N5 transition to σ* (C3–C4) with stabilization energy of 10.64 kJ/mol;
- LP(1) N6 transition to π* (C1–O7) and π* (C4–N5)with stabilization energy of 29.65 and 22.18 kJ/mol, respectively;
- LP(2) O7 transition to σ* (C1–C2) and σ* (C1–N6)with stabilization energy of 20.05 and 27.22 kJ/mol, respectively;

- LP(2) O19 transition to σ* (C17–C18) and σ* (C18–C20) with stabilization energy of 23 and 20.82 kJ/mol, respectively;
- LP(2) F26 transition to σ* (C22–C23) and σ* (C23–C24) with stabilization energy of 7.22 and 7.15 kJ/mol, respectively;
- LP(3) F26 transition to π* (C22–C23)with stabilization energy of 21.7 kJ/mol.

Besides analyzing the natural hybrid orbitals of the title molecule, it can be seen that, in bond orbitals corresponding to π (C9–C10), π (C11–C12), and π (C13–C14), and π (C20–C21), π (C22–C23), and π (C24–C25), which form the ring structures I and II, respectively, the bond hybrids have a near 100% p-character. In addition, orbitals π* (C9–C10), π* (C11–C12), π* (C13–C14), and π* (C20–C21), π* (C22–C23), and π* (C24–C25) have a near 100% p-character. Thus, transitions between the π to π* orbitals of these bonds present in the ring system are mainly defined by the p orbital-character (Table S2 in Supplementary Materials).

3.7.3. Electron Localization Function (ELF)

The ELF values can be characterized using the 2D representation shown in Figure 10. The regions represented in red are the regions of space where the probability of finding a single electron or opposite spin pair behavior is strong, with an ELF value close to 1, while the regions represented in blue are the regions where Pauli repulsion is minimal, with an ELF value close to 0. It was observed that high-value ELF (represented by the red region) occurs for the lighter hydrogen atoms in the ring system and the side chain [65]. By examining the ELF values of nitrogen, the blue areas represent the regions with the lowest values. The carbon atoms also had very low ELF values. The red region represents the location of the electrons in the carbon–carbon bonds in comparison to the electrons in the carbon–hydrogen bonds represented by the green region (Figure 10). The carbon–nitrogen bonds in the structure depicted localization characterized by substantial red regions.
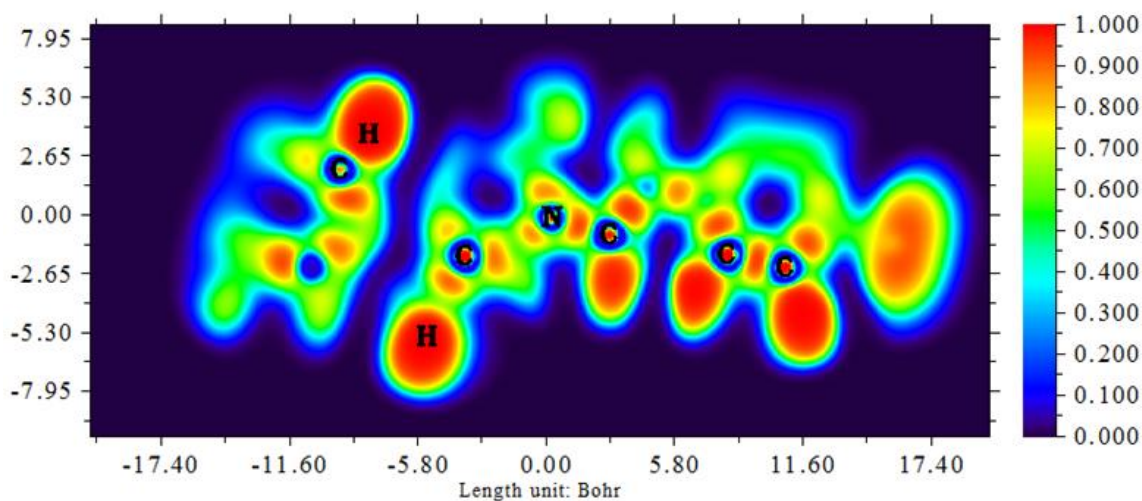

Figure 10. Color-filled ELF map of FOMMP in the molecular plane.

3.7.4. Molecular Electrostatic Potential Analysis

Site selectivity and reactivity analyses in terms of electrophilic and nucleophilic regions were conducted based on the 3D surfaces of MEP. This graphical representation reveals a repulsion region or a region of positive potential in blue, and the region of the negative potential of the title compound in red [66]. The red areas indicate electron-rich regions with negative values of the electrostatic potential. In the case of FOMMP, the most electronegative area is composed of nitrogen and oxygen atoms. The blue tones represent electron deficiency, which was observed in benzene ring I and II of the compound. The hydrogen and carbon atoms (focusing on areas of carbon) showed an area of higher electropositive behavior (Figure 11).
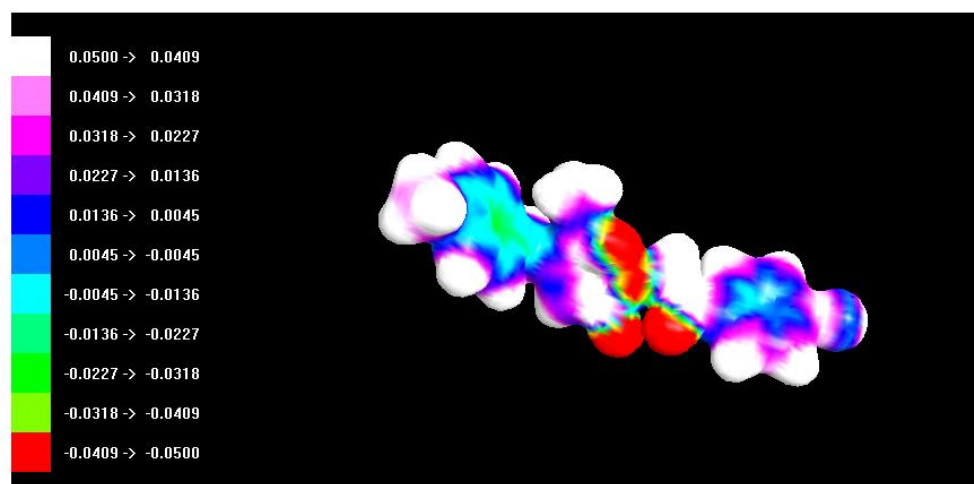
Figure 11. MEP plot of FOMMP.

3.7.5. Molecular Docking and Drug-Likeness Studies

Calculating the drug-likeness parameters for a molecule helps identify its oral bioavailability and absorption rates. For drug candidates, the initial classification must take into account the famous Lipinski rule [67,68]. The AlogP in the case of the FOMMP represented in Table 6 is equal to 4.01, which is lower than the threshold of 5. This parameter helps indicate the lipophilicity/hydrophobicity of the title molecule, which suggests that FOMMP could be considered as a leading drug candidate. Other conditions were also satisfied, such as HBA and HBD, which must be 10 and 5, respectively. According to Ghose et al. [69], the PSA was lower than 140 Å^2, molar refractivity was within the range of 40 and 130, and the number of rotatable bonds was also within the required range, further underlining the pharmaceutical potential of FOMMP.

Table 6. Drug-likeness parameters of FOMMP.

Descriptor	Values
Hydrogen bond donor (HBD)	4
Hydrogen bond acceptor (HBA)	0
AlogP	4.01
Polar surface area (PSA) [Å^2]	51.96
Molar refractivity	98.82
Number of rotatable bonds	5

Docking aids in identifying the highest energy of the binding site of a ligand to its receptor in relation to the binding energy. The aim of this docking study was to determine the interaction modes of the title ligand (FOMMP) with the protein 5R82, i.e., SARS-CoV-2's main protease with a cocrystallized structure, and thus investigate its potential as an antiviral drug [70].

The AutoDock software implements the Lamarckian genetic algorithm (LGA). The AGL is powerful because it adds local minimization to the genetic algorithm and, thus, allows the gene population to be modified. The binding free energy of the best conformation was estimated at −4.90 kcal/mol, and Table 7 shows the binding residues. The interaction modes diagram of the title ligand with the target receptor is shown in Figure 12 [71]. The ligand was embedded in the active site of the selected protein, and from the binding energy, we found that the ligand can bind easily with the desired protein to produce a postbinding effect.

Table 7. Hydrogen bonding and molecular docking of FOMMP with 5R82 protein target.

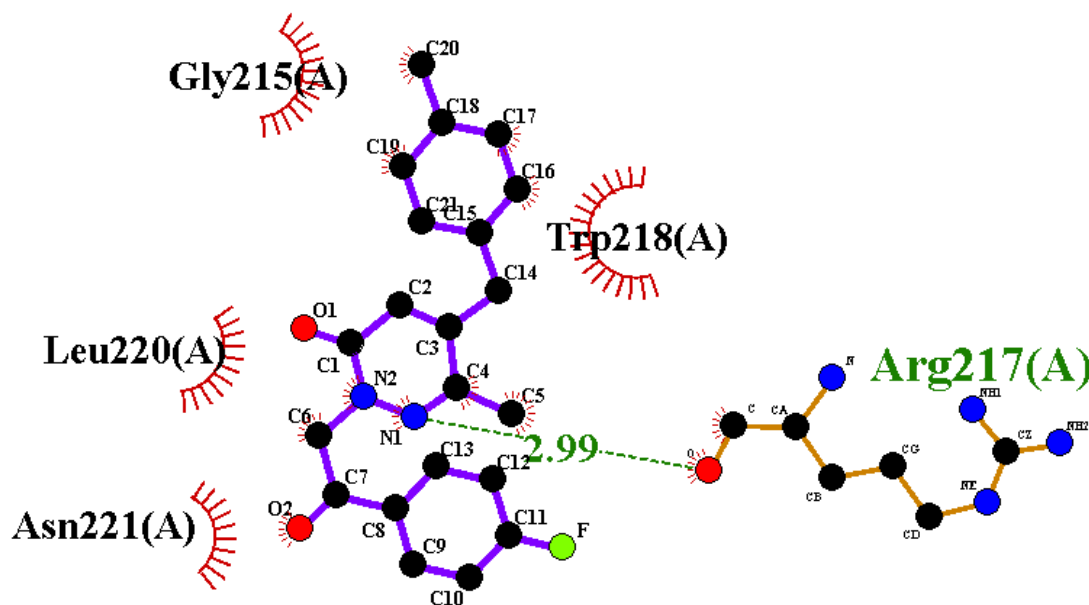| Ligand	Protein PDB ID	Binding Amino Acid Residues	Bond Distance (Å)	Binding Energy (kcal/mol)	Inhibition Constants (uM)
FOMMP	5R82	Arg217(A)	2.99	−4.90	257.64

Figure 12. FOMMP embedded in the active site of 5R82 protein (3D representation).

4. Conclusions

In summary, a new pyridazin-3(2*H*)-one derivative, 2-(2-(4-fluorophenyl)-2-oxoethyl)-6-methyl-5-(4-methylbenzyl)pyridazin-3(2*H*)-one (FOMMP), was synthesized and characterized using experimental techniques involving FT-IR, UV-Vis, ¹H-NMR, ¹³C-NMR, ESI-MS, and single-crystal X-ray diffraction analysis and theoretical techniques involving DFT and molecular docking analysis. From the FMO analysis, the η value showed that it is not a very hard molecule and, thus, is associated with greater reactivity. The ω value in this molecule falls in a region that suggests it is biologically active. The theoretically attained UV-spectrum in the solvent phase shows the excitation mode with a maximum absorption wavelength corresponding to 359.45 nm. According to MEP, nitrogen and oxygen were identified as the most significant reactive centers. Transitions with high stabilization energies correspond to orbitals (C9–C10), (C11–C12), and (C13–C14), and (C20–C21), (C22–C23), and (C24–C25), which form the ring structures I and II, respectively. In addition, the molecular docking results ascertained the binding relationship between the FOMMP and protein 5R82. Thus, it was indicated that FOMMP could be exploited as an excellent target to develop drugs against COVID-19 by targeting SARS-CoV-2's main protease.

Author Contributions: Conceptualization, F.E.K.; methodology, F.E.K. and C.S.A.; software, C.S.A.; formal analysis, S.K. and N.D.; resources, A.O.; writing—original draft preparation, K.K., C.S.A. and S.K.; visualization, S.M. and J.C.P.; writing—review and editing, K.K., H.A.A. and R.A.-S.; funding acquisition, H.A.A. and R.A.-S.; supervision, N.B. All authors have read and agreed to the published version of the manuscript.

References

1. Flefel, E.M.; Tantawy, W.A.; El-Sofany, W.I.; El-Shahat, M.; El-Sayed, A.A.; Abd-Elshafy, D.N. Synthesis of some new pyridazine derivatives for anti-HAV evaluation. *Molecules* **2017**, *22*, 148. [CrossRef] [PubMed]

2. Li, D.; Zhan, P.; Liu, H.; Pannecouque, C.; Balzarini, J.; De Clercq, E.; Liu, X. Synthesis and biological evaluation of pyridazine derivatives as novel HIV-1 NNRTIs. *Bioorg. Med. Chem.* **2013**, *21*, 2128–2134. [CrossRef] [PubMed]

3. Singh, B.; Bhatia, R.; Pani, B.; Gupta, D. Synthesis, crystal structures and biological evaluation of new pyridazine derivatives. *J. Mol. Struct.* **2020**, *1200*, 127084. [CrossRef]

4. Daoui, S.; Direkel, Ş.; Ibrahim, M.M.; Tüzün, B.; Chelfi, T.; Al-Ghorbani, M.; Karrouchi, K. Synthesis, Spectroscopic Characterization, Antibacterial Activity, and Computational Studies of Novel Pyridazinone Derivatives. *Molecules* **2023**, *28*, 678. [CrossRef]

5. Mantu, D.; Luca, M.C.; Moldoveanu, C.; Zbancioc, G.; Mangalagiu, I.I. Synthesis and antituberculosis activity of some new pyridazine derivatives. Part II. *Eur. J. Med. Chem.* **2010**, *45*, 5164. [CrossRef] [PubMed]

6. Ahmed, E.M.; Kassab, A.E.; El-Malah, A.A.; Hassan, M.S. Synthesis and biological evaluation of pyridazinone derivatives as selective COX-2 inhibitors and potential anti-inflammatory agents. *Eur. J. Med. Chem.* **2019**, *171*, 25–37. [CrossRef]

7. Barberot, C.; Moniot, A.; Allart-Simon, I.; Malleret, L.; Yegorova, T.; Laronze-Cochard, M.; Gérard, S. Synthesis and biological evaluation of pyridazinone derivatives as potential anti-inflammatory agents. *Eur. J. Med. Chem.* **2018**, *146*, 139–146. [CrossRef]

8. Rafi, U.M.; Mahendiran, D.; Devi, V.G.; Doble, M.; Rahiman, A.K. Pyridazine-based heteroleptic copper (II) complexes as potent anticancer drugs by inducing apoptosis and S-phase arrest in breast cancer cell. *Inorg. Chim. Acta* **2018**, *482*, 160–169. [CrossRef]

9. Livermore, D.G.; Bethell, R.C.; Cammack, N.; Hancock, A.P.; Hann, M.M.; Green, D.V.; Orr, D.C. Synthesis and anti-HIV-1 activity of a series of imidazo [1, 5-b] pyridazines. *J. Med. Chem.* **1993**, *36*, 3784–3794. [CrossRef]

10. Zerroug, A.; Belaidi, S.; BenBrahim, I.; Sinha, L.; Chtita, S. Virtual screening in drug-likeness and structure/activity relationship of pyridazine derivatives as Anti-Alzheimer drugs. *J. King Saud Univ. Sci.* **2018**, *31*, 595–601. [CrossRef]

11. Demirayak, S.; Karaburun, A.C.; Beis, R. Some pyrrole substituted aryl pyridazinone and phthalazinone derivatives and their antihypertensive activities. *Eur. J. Med. Chem.* **2004**, *39*, 1089–1095. [CrossRef]

12. Partap, S.; Akhtar, M.J.; Yar, M.S.; Hassan, M.Z.; Siddiqui, A.A. Pyridazinone hybrids: Design, synthesis and evaluation as potential anticonvulsant agents. *Bioorg. Chem.* **2018**, *77*, 74–83. [CrossRef]

13. Jacomini, A.P.; da Silva, M.J.; Poletto, J.; Ribeiro, G.M.; Yokoyama, J.T.; Bidóia, D.L.; Rosa, F.A. Potential antileishmanial activity of 4-N-Acylhydrazone Pyrazolo [3, 4-d] pyridazin-7-ones: Synthesis, in vitro biological evaluations and computational studies. *J. Braz. Chem. Soc.* **2018**, *29*, 2657–2668. [CrossRef]

14. Lümmen, P. Complex I inhibitors as insecticides and acaricides. *Biochim. Biophys. Acta Bioenerg.* **1998**, *1364*, 287–296. [CrossRef]

15. Dekeyser, M.A. Acaricide mode of action. *Pest. Manag. Sci.* **2005**, *61*, 103–110. [CrossRef]

16. Weissmuller, J.; Tietjen, K.G.; Stendel, W.; Wachendorff-Neumann, U. U. S. Patent No. 5,004,744, CI. 514-247.000; U.S. Patent and Trademark Office: Washington, DC, USA, 1991.

17. Asif, M. Antifeedant, herbicidal and molluscicidal activities of pyridazinone compounds. *Mini-Rev. Org. Chem.* **2013**, *10*, 113–122. [CrossRef]

18. Abraham, C.S.; Prasana, J.C.; Muthu, S. Quantum mechanical, spectroscopic and docking studies of 2-amino-3-bromo-5-nitropyridine by density functional method. *Spectrochim. Acta A* **2017**, *181*, 153–163. [CrossRef]

19. Pillai, R.R.; Karrouchi, K.; Fettach, S.; Armaković, S.; Armaković, S.J.; Brik, Y.; Faouzi, M.E.A. Synthesis, spectroscopic characterization, reactive properties by DFT calculations, molecular dynamics simulations and biological evaluation of Schiff bases tethered 1, 2, 4-triazole and pyrazole rings. *J. Mol. Struct.* **2019**, *1177*, 47–54. [CrossRef]

20. Tighadouini, S.; Radi, S.; Abrigach, F.; Benabbes, R.; Eddike, D.; Tillard, M. Novel β-keto–enol pyrazolic compounds as potent antifungal agents. Design, synthesis, crystal structure, DFT, homology modeling, and docking studies. *J. Chem. Inf. Model.* **2019**, *59*, 1398–1409. [CrossRef]

21. Karrouchi, K.; Yousfi, E.B.; Sebbar, N.K.; Ramli, Y.; Taoufik, J.; Ouzidan, Y.; Radi, S. New pyrazole-hydrazone derivatives: X-ray analysis, molecular structure investigation via density functional theory (DFT) and their high in-situ catecholase activity. *Int. J. Mol. Sci.* **2017**, *18*, 2215. [CrossRef]

22. Abraham, C.S.; Muthu, S.; Prasana, J.C.; Rizwana, B.F.; Armaković, S.; Armaković, S.J. Vibrational and electronic absorption spectroscopic profiling, natural hybrid orbital, charge transfer, electron localization function and molecular docking analysis on 3-amino-3-(2-nitrophenyl) propionic acid. *J. Mol. Struct.* **2018**, *1171*, 733–746. [CrossRef]

23. Abraham, C.S.; Muthu, S.; Prasana, J.C.; Armaković, S.J.; Armaković, S.; AS, B.G. Spectroscopic profiling (FT-IR, FT-Raman, NMR and UV-Vis), autoxidation mechanism (H-BDE) and molecular docking investigation of 3-(4-chlorophenyl)-N, N-dimethyl-3-pyridin-2-ylpropan-1-amine by DFT/TD-DFT and molecular dynamics: A potential SSRI drug. *Comput. Biol. Chem.* **2018**, *77*, 131–145. [CrossRef] [PubMed]

24. Bouzian, Y.; Karrouchi, K.; Sert, Y.; Lai, C.H.; Mahi, L.; Ahabchane, N.H.; Essassi, E.M. Synthesis, spectroscopic characterization, crystal structure, DFT, molecular docking and in vitro antibacterial potential of novel quinoline derivatives. *J. Mol. Struct.* **2020**, *1209*, 127940. [CrossRef]

25. El Kalai, F.; Çınar, E.B.; Lai, C.H.; Daoui, S.; Chelfi, T.; Allali, M.; Benchat, N. Synthesis, spectroscopy, crystal structure, TGA/DTA study, DFT and molecular docking investigations of (E)-4-(4-methylbenzyl)-6-styrylpyridazin-3 (2H)-one. *J. Mol. Struct.* **2021**, *1228*, 12943. [CrossRef]

26. Daoui, S.; Faizi, M.S.H.; Kalai, F.E.; Saddik, R.; Dege, N.; Karrouchi, K.; Benchat, N. Crystal structure and the DFT and MEP study of 4-benzyl-2-[2-(4-fluorophenyl)-2-oxoethyl]-6-phenylpyridazin-3 (2H)-one. *Acta Cryst.* **2019**, *E75*, 1030. [CrossRef]

27. El Kalai, F.; Baydere, C.; Daoui, S.; Saddik, R.; Dege, N.; Karrouchi, K.; Benchat, N. Crystal structure and Hirshfeld surface analysis of ethyl 2-[5-(3-chlorobenzyl)-6-oxo-3-phenyl-1, 6-dihydropyridazin-1-yl] acetate. *Acta Cryst.* **2019**, *E75*, 892–895. [CrossRef]

28. Dadou, S.; Kansiz, S.; Daoui, S.; El Kalai, F.; Baydere, C.; Saddik, R.; Benchat, N. Crystal structures and Hirshfeld surface analyses of 4-benzyl-6-phenyl-4, 5-dihydropyridazin-3 (2H)-one and methyl 2-[5-(2, 6-dichlorobenzyl)-6-oxo-3-phenyl-1, 4, 5, 6-tetrahydropyridazin-1-yl] acetate. *Acta Cryst.* **2019**, *E75*, 1679–1684. [CrossRef] [PubMed]

29. El Kalai, F.; Chelfi, T.; Benchat, N.; Bouklah, M.; Daoui, S.; Karrouchi, K.; Ben Hadda, T. New heterocyclic compounds based on pyridazinones scaffold as efficient inhibitor of corrosion of mild steel in acidic solution 1 M HCl. *J. Bio-Tribo-Corros.* **2020**, *6*, 89. [CrossRef]

30. Bruker. *APEX3, SAINT, SADABS & SHELXTL*; Bruker AXS, Inc.: Madison, WI, USA, 2016.

31. Sheldrick, G.M. SHELXT–Integrated space-group and crystal-structure determination. *Acta Cryst.* **2015**, *A71*, 3–8. [CrossRef]

32. Sheldrick, G.M. Crystal structure refinement with SHELXL. *Acta Cryst.* **2015**, *C71*, 3–8.

33. Brandenburg, K.; Berndt, M. *DIAMOND*; Crystal Impact GbR: Bonn, Germany, 2012.

34. Frisch, M.J.; Trucks, G.W.; Schlegel, H.B.; Scuseria, G.E.; Robb, M.A.; Cheeseman, J.R.; Montgomery, J.A., Jr.; Vreven, T.; Kudin, K.N.; Burant, J.C.; et al. *Gaussian 09, Revision E.01*; Gaussian, Inc: Wallingford, CT, USA, 2004.

35. Becke, A. Density-functional thermochemistry. III. The role of exact exchange. *J. Chem. Phys.* **1993**, *98*, 5648–5656. [CrossRef]

36. O'boyle, N.M.; Tenderholt, A.L.; Langner, K.M. Cclib: A library for package-independent computational chemistry algorithms. *J. Comp. Chem.* **2008**, *29*, 839–845. [CrossRef]

37. *Schrödinger Release 2018-1: Maestro*; Schrödinger, LLC: New York, NY, USA, 2018.

38. Sanner, M.F. Python: A programming language for software integration and development. *J. Mol. Graph. Mod.* **1999**, *17*, 57.

39. Stoe, C. *X-AREA (Version 1.18) and X-RED (Version 1.04)*; Stoe & Cie: Darmstadt, Germany, 2002.

40. Bak, B.; Christensen, D.; Dixon, W.B.; Hansen-Nygaard, L.; Rastrup-Andersen, J. Benzene ring distortion by one substituent. microwave determination of the complete structure of benzonitrile. *J. Chem. Phys.* **1962**, *37*, 2027. [CrossRef]

41. Bailey, A.S.; Prout, C.K. 899. Molecular complexes. Part III. The crystal and molecular structure of the 1:2 molecular compound of bis-8-hydroxyquinolinatocopper (II) and picryl azide. *J. Chem. Soc* **1965**, 4867–4881. [CrossRef]

42. Schomaker, V.T.; Pauling, L. The electron diffraction investigation of the structure of benzene, pyridine, pyrazine, butadiene-1, 3, cyclopentadiene, furan, pyrrole, and thiophene. *J. Am. Chem. Soc.* **1939**, *61*, 1769. [CrossRef]

43. James, M.N.G.; Williams, G.J.B. Structural studies of histamine H1 effector molecules: The crystal structure of the antihistamine drug (+)-chlorpheniramine maleate;[(+)-S-1-(p-chlorophenyl)-1-(2-pyridyl)-3-N, N-dimethylpropylamine maleate]. *J. Chem.* **1974**, *52*, 1872–1879. [CrossRef]

44. Srinivasan, R. On the method of least squares as applied to the refinement of crystal structures. *Acta Cryst.* **1961**, *14*, 1163–1167. [CrossRef]

45. Karrouchi, K.; Brandán, S.A.; Sert, Y.; El-Marzouqi, H.; Radi, S.; Ferbinteanu, M.; Garcia, Y. Synthesis, X-ray structure, vibrational spectroscopy, DFT, biological evaluation and molecular docking studies of (E)-N′-(4-(dimethylamino) benzylidene)-5-methyl-1H-pyrazole-3-carbohydrazide. *J. Mol. Struct.* **2020**, *1219*, 128541. [CrossRef]

46. Karrouchi, K.; Brandán, S.A.; Sert, Y.; El Karbane, M.; Radi, S.; Ferbinteanu, M.; Garcia, Y. Synthesis, structural, molecular docking and spectroscopic studies of (E)-N′-(4-methoxybenzylidene)-5-methyl-1H-pyrazole-3-carbohydrazide. *J. Mol. Struct.* **2021**, *1225*, 129072. [CrossRef]

47. Karrouchi, K.; Brandán, S.A.; Hassan, M.; Bougrin, K.; Radi, S.; Ferbinteanu, M.; Garcia, Y. Synthesis, X-ray, spectroscopy, molecular docking and DFT calculations of (E)-N′-(2, 4-dichlorobenzylidene)-5-phenyl-1H-pyrazole-3-carbohydrazide. *J. Mol. Struct.* **2021**, *1228*, 129714. [CrossRef]

48. Karrouchi, K.; Fettach, S.; Jotani, M.M.; Sagaama, A.; Radi, S.; Ghabbour, H.A.; Issaoui, N. Synthesis, crystal structure, hirshfeld surface analysis, DFT calculations, anti-diabetic activity and molecular docking studies of (E)-N′-(5-bromo-2-hydroxybenzylidene) isonicotinohydrazide. *J. Mol. Struct.* **2020**, *1221*, 128800. [CrossRef]

49. Daoui, S.; Baydere, C.; Akman, F.; El Kalai, F.; Mahi, L.; Dege, N.; Benchat, N. Synthesis, X-ray crystallography, vibrational spectroscopy, thermal and DFT studies of (E)-6-(4-methylstyryl)-4, 5-dihydropyridazin-3 (2H)-one. *J. Mol. Struct.* **2021**, *1225*, 129180. [CrossRef]

50. El Kalai, F.; Karrouchi, K.; Baydere, C.; Daoui, S.; Allali, M.; Dege, N.; Brandan, S.A. Synthesis, crystal structure, spectroscopic studies, NBO, AIM and SQMFF calculations of new pyridazinone derivative. *J. Mol. Struct.* **2021**, *1223*, 129213. [CrossRef]

51. Spackman, M.A.; Byrom, P.G. A novel definition of a molecule in a crystal. *Chem. Phys. Lett.* **1997**, *267*, 215–2020. [CrossRef]

52. Demircioğlu, Z.; Kaştaş, G.; Kaştaş, Ç.A.; Frank, R. Spectroscopic, XRD, Hirshfeld surface and DFT approach (chemical activity, ECT, NBO, FFA, NLO, MEP, NPA& MPA) of (E)-4-bromo-2-[(4-bromophenylimino) methyl]-6-ethoxyphenol. *J. Mol. Struct.* **2019**, *1191*, 129–137.

53. Uzun, S.; Demircioğlu, Z.; Taşdoğan, M.; Ağar, E. Quantum chemical and X-ray diffraction studies of (E)-3-(((3, 4-dimethoxybenzyl) imino) methyl) benzene-1, 2-diol. *J. Mol. Struct.* **2020**, *1206*, 127749. [CrossRef]

54. Padmaja, L.; Ravikumar, C.; Sajan, D.; Joe, I.H.; Jayakumar, V.S.; Pettit, G.R.; Neilsen, F.O. Density functional study on the structural conformations and intramolecular charge transfer from the vibrational spectra of the anticancer drug combretastatin-A2. *J. Raman. Spectrosc.* **2020**, *40*, 419–428. [CrossRef]

55. Ravikumar, C.; Joe, I.H.; Jayakumar, V.S. Charge transfer interactions and nonlinear optical properties of push–pull chromophore benzaldehyde phenylhydrazone: A vibrational approach. *Chem. Phys. Lett.* **2008**, *460*, 552–558. [CrossRef]

56. Zhou, Z.; Parr, R.G. Activation hardness: New index for describing the orientation of electrophilic aromatic substitution. *J. Am. Chem. Soc.* **1990**, *112*, 5720–5724. [CrossRef]

57. Pearson, R.G. Recent advances in the concept of hard and soft acids and bases. *J. Chem. Ed.* **1987**, *64*, 561. [CrossRef]

58. Parr, R.G.; Yang, W. *Density Functional Theory of Atoms and Molecules*; Oxford University Press: Oxford, UK, 1989.

59. Yang, W.; Parr, R.G. Hardness, softness, and the fukui function in the electronic theory of metals and catalysis. *Proc. Natl. Acad. Sci. USA* **1985**, *82*, 6723–6726. [CrossRef] [PubMed]

60. Parr, R.G.; Pearson, R.G. Absolute hardness: Companion parameter to absolute electronegativity. *J. Am. Chem. Soc.* **1983**, *105*, 7512–7516. [CrossRef]

61. Kovačević, N.; Kokalj, A. Analysis of molecular electronic structure of imidazole-and benzimidazole-based inhibitors: A simple recipe for qualitative estimation of chemical hardness. *Corros. Sci.* **2011**, *53*, 909–921. [CrossRef]

62. Geerlings, P.; De Proft, F.; Langenaeker, W. Conceptual density functional theory. *Chem. Rev.* **2003**, *103*, 1793–1874. [CrossRef]

63. Parthasarathi, R.; Subramanian, V.; Roy, D.R.; Chattaraj, P.K. Electrophilicity index as a possible descriptor of biological activity. *Bioorg. Med. Chem.* **2004**, *12*, 5533. [CrossRef]

64. Guido, C.A.; Cortona, P.; Mennucci, B.; Adamo, C. On the metric of charge transfer molecular excitations: A simple chemical descriptor. *J. Chem. Theory Comput.* **2013**, *9*, 3118–3126. [CrossRef]

65. Mandal, S.; Nandi, S.; Anoop, A.; Chattaraj, P.K. Viability of aromatic all-pnictogen anions. *Phys. Chem. Chem. Phys.* **2016**, *18*, 11738–11745. [CrossRef]

66. Williams, D.E. Comprehensive Chemical Kinetics. *Rev. Comp. Chem.* **1991**, *2*, 226.

67. Lipinski, C.A.; Lombardo, F.; Dominy, B.W.; Feeney, P.J. Experimental and computational approaches to estimate solubility and permeability in drug discovery and development settings. *Adv. Drug Deliv. Rev.* **1997**, *23*, 4–17. [CrossRef]

68. Lipinski, C.A. Lead-and drug-like compounds: The rule-of-five revolution. *Drug Discov. Today Technol.* **2004**, *1*, 337–341. [CrossRef] [PubMed]

69. Ghose, A.K.; Viswanadhan, V.N.; Wendoloski, J.J. A knowledge-based approach in designing combinatorial or medicinal chemistry libraries for drug discovery. 1. A qualitative and quantitative characterization of known drug databases. *J. Comb. Chem.* **1999**, *1*, 55. [CrossRef] [PubMed]

70. Fearon, D.; Powell, A.J.; Douangamath, A.; Protein Data Bank. *PanDDA Analysis Group Deposition—Crystal Structure of COVID-19 Main Protease in Complex with Z219104216*; Protein Data Bank Japan: Suita, Japan, 2020.

71. Wallace, A.C.; Laskowski, R.A.; Thornton, J.M. LIGPLOT: A program to generate schematic diagrams of protein-ligand interactions. *Protein Eng.* **1995**, *8*, 127–134. [CrossRef] [PubMed]